

Large-area bifacial n-TOPCon solar cells with in situ phosphorus-doped
LPCVD poly-Si passivating contacts

Peer-reviewed author version

FIRAT, Meric; Radhakrishnan, Hariharsudan Sivaramakrishnan; Payo, Maria Recaman; CHOULAT, Patrick; Badran, Hussein; VAN DER HEIDE, Arvid; GOVAERTS, Jonathan; DUERINCKX, Filip; TOUS, Loic; Hajjiah, Ali & POORTMANS, Jef (2022) Large-area bifacial n-TOPCon solar cells with in situ phosphorus-doped LPCVD poly-Si passivating contacts. In: Solar Energy Materials and Solar Cells, 236 (Art N° 111544).

DOI: 10.1016/j.solmat.2021.111544

Handle: <http://hdl.handle.net/1942/36960>

Large-Area Bifacial n-TOPCon Solar Cells with *In Situ* Phosphorus-Doped LPCVD Poly-Si Passivating Contacts

Meriç Firat^{a,b,*}, Hariharsudan Sivaramakrishnan Radhakrishnan^b, María Recamán Payo^c, Patrick Choulat^b, Hussein Badran^d, Arvid van der Heide^b, Jonathan Govaerts^b, Filip Duerinckx^b, Loic Tous^b, Ali Hajjiah^d, Jef Poortmans^{a,b,e}

^aKU Leuven, Department of Electrical Engineering, Kasteelpark Arenberg 10, 3001 Leuven, Belgium

^bImec (Partner in EnergyVille), Kapeldreef 75, 3001 Leuven, Belgium

^cKU Leuven, Department of Physics and Astronomy, Celestijnenlaan 200d, 3001 Leuven, Belgium

^dDepartment of Electrical Engineering, College of Engineering and Petroleum, Kuwait University, 13133 Safat, Kuwait

^eUHasselt, Campus Diepenbeek, Agoralaan Gebouw D, 3590 Diepenbeek, Belgium

*Corresponding author: meric.firat@imec.be

Abstract – The potential of passivating contacts incorporating *in situ* phosphorus (P)-doped polycrystalline silicon (poly-Si) films grown by low pressure chemical vapor deposition (LPCVD) is demonstrated in this work by integrating these layers at the rear side of large-area (241.3 cm²) bifacial n-type Tunnel Oxide Passivated Contact (n-TOPCon) solar cells with diffused front emitter and screen-printed contacts. *In situ* doped poly-Si films are studied as their use could simplify the production of industrial n-TOPCon solar cells compared to the common approach relying on *ex situ* doping of intrinsic LPCVD poly-Si films. The developed poly-Si passivating contacts exhibited excellent characteristics with low recombination current densities in passivated and screen-printing metallized regions down to 2.3 fA/cm² and 65.8 fA/cm², respectively, and a low contact resistivity of 2.0 mΩ·cm². For reaching the best passivating contact characteristics and high solar cell efficiencies, a poly-Si film thickness of 150-200 nm was found to be optimal while a polished rear surface morphology was found to be beneficial. The best solar cell reached a certified power conversion efficiency of 23.01% along with a high open circuit voltage of 691.7 mV, enabled by the passivating contacts with the *in situ* doped poly-Si films. 1-cell glass-glass laminates were also fabricated with the developed solar cells, which showed no loss in their power output both upon 400 thermal cycles and after 1000 hours of damp heat testing. Lastly, a roadmap is presented, indicating strategies to achieve efficiencies up to 25.5% with n-TOPCon solar cells incorporating the *in situ* P-doped LPCVD poly-Si films.

Keywords – passivating contacts, TOPCon, solar cells, polysilicon, LPCVD, *in situ* phosphorus doping

1 Introduction

In recent years, n-type Tunnel Oxide Passivated Contact (n-TOPCon) solar cells have found increased interest and market share in the field of photovoltaics (PV) [1]. The appeal of n-TOPCon solar cells is in the incorporation of rear passivating contacts consisting of n-type polycrystalline silicon (poly-Si) and interfacial SiO_x films, which provide low recombination current density (J_0) and contact resistivity (ρ_c) simultaneously [2]. The potential of the n-TOPCon technology has already been demonstrated by the achievement of a record power conversion efficiency (η) of 25.8% with a lab-type small-area solar cell [3], impressive η up to 25.4% with large-area solar cells [4–6], and a high average η exceeding 24% in production [7,8].

In the PV community, a vast body of research has been devoted to the development and device integration of poly-Si passivating contacts, based on various fabrication techniques [2,9,10]. For the fabrication of the poly-Si films used in industrial n-TOPCon solar cells, low pressure chemical vapor deposition (LPCVD) has been the primary choice so far [1]. The PV industry has favored this technique because of its high throughput and since LPCVD equipment offers the possibility of thermally growing the interfacial SiO_x film *in situ* [2]. While the latter feature allows process simplification by combining the deposition of the SiO_x and the Si, deposited either as poly-Si or as amorphous Si (a-Si), layers in a single step, current LPCVD-based approaches in the PV industry still do not exploit the full potential of this technique in terms of process simplicity. This is because the necessary phosphorus (P) doping of the Si film is realized by an *ex situ* method, usually dopant diffusion, after LPCVD of intrinsic Si, which makes the fabrication of the passivating contact inherently a two-step process [2]. By contrast, an alternative approach based on *in situ* doping can allow producing the entire passivating contact in a single step, offering the possibility of leaner fabrication.

Device integration of poly-Si passivating contacts fabricated by the standard industrial approach based on LPCVD and *ex situ* P doping has been the focus of a plethora of studies [2,5,10,11]. As a result, the impact of various n-TOPCon solar cell design parameters on the *ex situ* doped passivating contact and device properties has already been investigated. The studied parameters include the method used for growing the interfacial SiO_x film [12], the structural properties of the poly-Si film [13], the poly-Si film thickness (t_{poly}) [14,15], and the composition of the screen-printing paste used for the metallization of the passivating contact

[16]. Related to the alternative approach for the fabrication of poly-Si films based on LPCVD and *in situ* P doping, various studies are present in the literature, which provide valuable insights into the impact of LPCVD process parameters on structural and electrical properties of poly-Si films [17–22]. Nevertheless, the applications considered in these studies are mainly not associated with PV. In fact, the number of publications on the fabrication of industrial n-TOPCon solar cells with *in situ* P-doped LPCVD poly-Si films has been limited due to challenges arising from combining LPCVD with *in situ* P-doping, which has made *ex situ* doping the preference of the PV industry so far [23–25]. The main challenge is to achieve a high active doping level ($N_{D,act}$) in the deposited Si film, which is needed for obtaining low J_0 and ρ_c , together with a high deposition rate (r_{dep}) and thus throughput, as P-containing precursors slow down the Si film growth [17].

A process offering an optimized trade-off between these parameters has recently been developed by our group, which achieves the deposition of Si films, in polycrystalline form, with a high $N_{D,act}$ of $1.3 \cdot 10^{20} \text{ cm}^{-3}$ and an r_{dep} of 0.078 nm/s [26]. This represents a ~53% drop in r_{dep} with respect to the LPCVD of intrinsic Si at the same temperature (590°C), which corresponds to an increase of the time required for the deposition of a typical 150 nm thick Si film by only ~17 min, from ~15 min for the growth of intrinsic poly-Si to ~32 min in case of *in situ* doping [26]. Moreover, by combining the poly-Si films developed in our previous work with thermally grown interfacial SiO_x layers and applying post-LPCVD annealing, excellent passivating contacts were fabricated with J_0 down to 1.5 fA/cm² and ρ_c down to 1.8 mΩ·cm² [26]. The potential of these passivating contacts is assessed in this work at device level.

It is important to note that the use of thermal annealing, which is considered necessary for the activation of dopants and commonly applied to *in situ* doped Si films [2], makes the *in situ* doping-based approach a two-step process itself as in the case of *ex situ* doping by dopant diffusion. However, it has been shown in the literature that, while the deposition of *in situ* doped Si films is more expensive than their intrinsic counterparts due to the reduced r_{dep} in case of *in situ* doping, the overall cost of ownership of n-TOPCon solar cells incorporating *in situ* doped poly-Si passivating contacts can be lower by 0.2 \$cents per Watt peak than the devices with conventional *ex situ* doped passivating contacts, if the annealing in case of *in situ* doping can be optimized to yield a shorter and leaner process [17,27]. Moreover, a simpler single-step process may still be achieved in case of *in situ* doping either by developing LPCVD equipment which can perform the annealing also *in situ*, or by means of the fired passivating

contact concept, which eliminates the annealing and relies on the firing step used for screen-printed metallization also for the activation of dopants in the Si film [28]. However, these developments are beyond the scope of this work.

This paper reports on the integration of passivating contacts based on *in situ* P-doped poly-Si films by LPCVD at the rear side of large-area bifacial n-TOPCon solar cells. The devices were fabricated relying on industrial methods, using a homogeneous boron-diffused front emitter and screen-printed metallization. Impact of t_{poly} on the passivating contact and the solar cell properties is presented. Moreover, performance of the passivating contacts and the solar cells are reported for two types of rear surface morphologies: semi-textured and polished. The paper also reports on the suitability of the developed solar cells for application in PV modules by means of thermal cycling and damp heat tests. In addition, a roadmap is provided which shows how the efficiency of n-TOPCon solar cells featuring *in situ* P-doped poly-Si films by LPCVD can be further improved starting from the baseline established in this work.

2 Materials and Methods

2.1 Integration of *In Situ* Doped LPCVD Poly-Si Passivating Contacts in n-TOPCon Solar Cells

The *in situ* P-doped LPCVD-based poly-Si films developed in [26] were integrated in n-TOPCon solar cells in two sets of experiments. The goal of the first experiment was to study the impact of t_{poly} on the solar cell performance and identify the optimal t_{poly} value. This experiment is referred to as the t_{poly} screening experiment. For this purpose, solar cells with a large area of 241.3 cm² were prepared using n-type Cz wafers with the structure illustrated in Fig. 1a), following the process flow in Fig. 1b). After random pyramid texturing and cleaning, a ~ 1 μm -deep homogeneous p-type emitter with a sheet resistance of 110 Ω/\square was realized by BBr₃ diffusion, followed by the removal of the borosilicate glass (BSG) in a solution containing diluted hydrofluoric acid (HF). The boron-diffused layer was later removed from the rear side by the so-called emitter removal process using a mixture of 49% HF, 70% nitric acid (HNO₃), and concentrated sulfuric acid (H₂SO₄), with volume concentrations of 6.2%, 36.0%, and 21.4%, respectively, in the mixture diluted in water [29]. This is a single-side etching process performed in a Rena inline processing equipment with the wafers moving at 8°C on closely spaced rollers with a speed of 1.5 m/min over etch baths overflowed with the aforementioned chemistry. The process consists of two passes of each wafer through the equipment, leading to

the removal of $\sim 1.5\text{-}2\ \mu\text{m}$ of Si from the rear determined by weight measurements, resulting in a semi-textured surface morphology with slightly rounded-off pyramids.

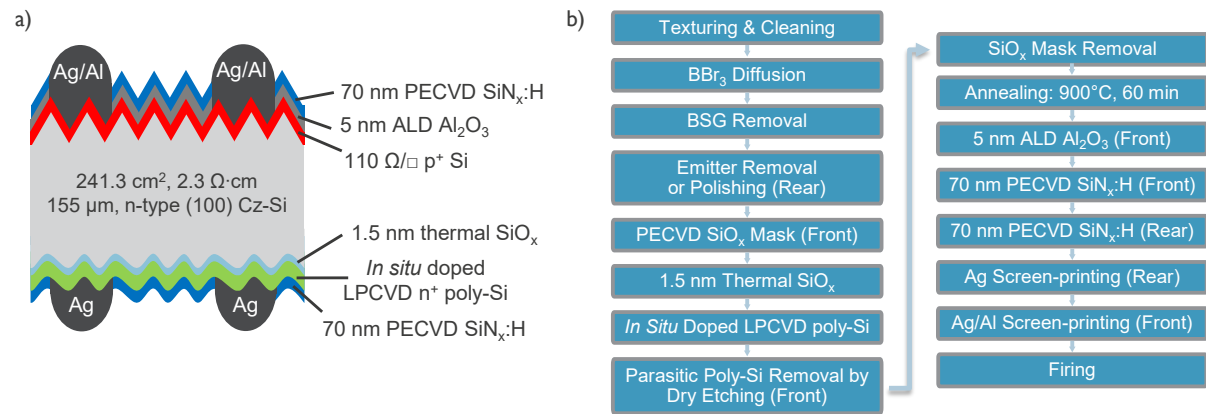


Figure 1. a) Schematic (not drawn to scale) of the large-area bifacial n-TOPCon solar cells with a homogeneous diffused front emitter and screen-printed contacts. b) Process flow followed for fabricating the solar cells in a).

The fabrication continued with the realization of the poly-Si passivating contact on the rear. For this, first, the front side was masked with a 200 nm thick SiO_x mask grown by plasma enhanced chemical vapor deposition (PECVD) in a batch-type system. Later, the interfacial SiO_x layer of the passivating contact structure was grown thermally, yielding a thickness of $\sim 1.5\ \text{nm}$ measured by transmission electron microscopy (TEM) on identically oxidized thickness monitors. We would like to note that the monitors had been annealed by the same process as the solar cells prior to the TEM measurements. Following the oxidation, the *in situ* P-doped poly-Si film was deposited by LPCVD in a single-wafer ASM Epsilon 2000 reactor, using the process reported in [26]. The split of the t_{poly} screening experiment was introduced at this step by varying the deposition duration, which resulted in three different t_{poly} values: 100 nm, 150 nm, and 200 nm. For each one of these thicknesses, a group of 8 solar cells was prepared. The t_{poly} values were confirmed for each split by scanning electron microscopy (SEM) measurements on identically processed thickness monitors. As for the oxide thickness monitors, the t_{poly} monitors had also undergone the same annealing process as the solar cells before the thickness measurements.

As the LPCVD process creates a wrap-around of poly-Si at the front surface, this parasitic layer was removed by a single-side dry etch process in NF_3 plasma, followed by the removal of the SiO_x mask in HF. The reader should note that, while dry etching was used in this work, wrap-around removal can also be performed by the simpler and more common approach based on

single-side wet-chemical etching of poly-Si in a diluted alkaline solution, eliminating the masking step [12,30,31]. Subsequently, the samples were annealed at 900°C for 60 min [26]. Afterwards, the front surface was passivated with 5 nm thick atomic layer deposited (ALD) AlO_x and 70 nm thick PECVD $\text{SiN}_x\text{:H}$ films, the latter of which also acts as an antireflection coating (ARC). A 70 nm thick PECVD $\text{SiN}_x\text{:H}$ film was also applied to the rear side for improving the passivation quality provided by the passivating contact by means of hydrogenation. Fabrication of the solar cells was then completed by metallization using a zero-busbar design on both sides, leading to bifacial solar cells. The metallization fraction of the front and rear surfaces of the solar cells was 2.7% and 5%, respectively. For metallization, Ag and Ag/Al pastes were screen-printed at the rear and front sides, respectively, followed by firing of the pastes through the $\text{SiN}_x\text{:H}$ films for realizing contacts with the poly-Si and the emitter. Firing was performed with a belt speed of 150 inches per minute and a set peak temperature of 855°C.

The focus of the second experiment was to investigate the impact of the rear surface morphology on the n-TOPCon solar cells. This experiment is referred to as the rear surface morphology screening experiment. For this, a reference group of 7 solar cells was prepared with the same design and process as for the t_{poly} screening experiment i.e., the rear surface morphology was semi-textured. For this reference group, a single t_{poly} value of 150 nm was chosen. In addition, another group of 14 solar cells was fabricated, also with $t_{\text{poly}} = 150$ nm but a polished rear surface morphology. The design of these solar cells is also the one depicted in Fig. 1a) and the fabrication followed the process flow in Fig. 1b), with the only difference to the reference group being the strength of the single-side etch used for removing the boron-diffused emitter from the rear side. Instead of the emitter removal process, a polishing process was applied to these solar cells using the same equipment as for emitter removal but a more concentrated HF/ HNO_3 mixture. In more detail, the volume concentrations of 49% HF and 70% HNO_3 in the polishing solution were 20% and 80%, respectively. The wafer speed was 1.5 m/min, identical to the emitter removal process, but the process temperature was slightly higher, at 12°C. The polishing process was applied a single time to each wafer, which removes ~6 μm of Si and yields a flatter rear surface, which, however, does not correspond to a mirror-polished surface but exhibits significant roughness [29]. Moreover, on four of the best solar cells of the rear surface morphology screening experiment, selected from the group with the polished rear surface, an additional 90 nm thick SiO_x layer was deposited by PECVD (in a

single-wafer system unlike the previous PECVD steps) on top of the front SiN_x:H film and the metal grid to create a double ARC (DARC) and to further reduce the front reflectance [32,33].

The solar cells of both experiments were characterized by current-voltage (I - V) measurements under 1 sun illumination with the AM1.5 G spectrum using a Wacom solar simulator and a GridTouch system by Pasan to contact the zero-busbar devices. These measurements were performed both with front and rear illumination. In case of the solar cells with a DARC, I - V measurements were repeated after the realization of the DARC, and the best solar cell was also sent to ISFH CalTeC for a calibrated I - V measurement. From the I - V measurements with front illumination, the open circuit voltage (V_{oc}), the short circuit current density (J_{sc}), the fill factor (FF), and the power conversion efficiency (η) of the solar cells were extracted. Moreover, the η values obtained with front and rear illumination were used for determining the bifaciality of the solar cells as the ratio of the rear and front η . Furthermore, the I - V measurements with front illumination were repeated with the illumination intensity reduced to 7% of 1 sun. The resulting data and the data acquired under 1 sun front illumination were used together for determining the ideality factor (n) and the area-normalized series resistance (r_s) by the Bowden method [34]. In addition, to gain insight into the FF losses, FF values without the impact of r_s (FF_n) and without the impact of both r_s and non-ideal n (FF_0) were calculated [34].

The solar cells were further inspected by optical microscopy to assess the quality of the screen-printed contacts. Moreover, the reflectance (R) and the external quantum efficiency (EQE) spectra of the devices were measured under front illumination at a 2 cm x 2 cm spot on the solar cell in the wavelength (λ) range of 280-1200 nm using a LOANA system by PV-tools with a black chuck. For the EQE measurements, a bias light of 0.3 suns was used. The EQE data was corrected by a wavelength-independent scaling factor so that its integration with the AM1.5 G spectrum yields the J_{sc} determined by the I - V measurements. These data were analyzed for understanding the differences in the optical performance of each group of solar cells.

For understanding the factors limiting the performance of the n-TOPCon solar cells, symmetrically passivated monitor samples were also prepared together with the devices. These rear and front monitors, depicted schematically in Fig. 2a) and 2b), respectively, were designed to reproduce either the rear or the front side of the devices, allowing the passivation and contact properties of each surface to be independently investigated. As the rear surface design was

varied during the experiments, a set of two rear monitors was fabricated for each t_{poly} and rear surface morphology studied. By contrast, the front surface remained the same in all experiments, thus only two front monitors were prepared. Fabrication of the monitors followed the relevant steps in the process flow shown in Fig. 1b). On the monitors, the metal fingers were screen-printed only on some regions and with varying metallization fraction, while other regions were left non-metallized [26].

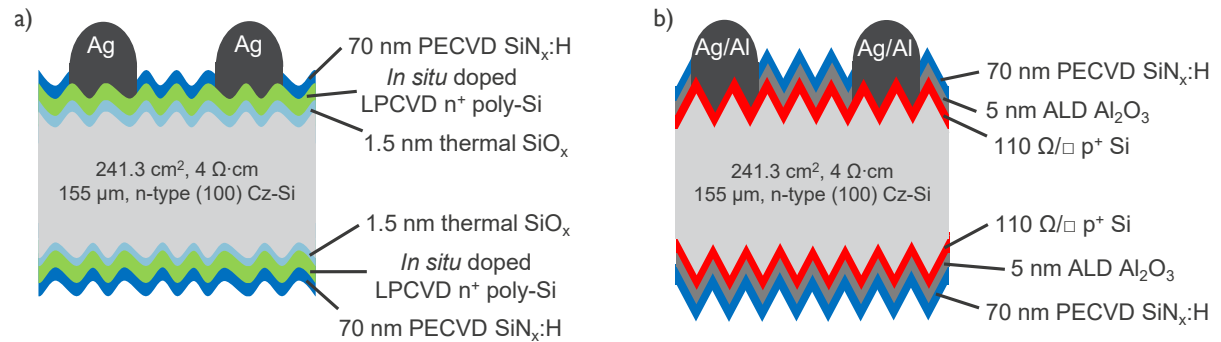


Figure 2. Schematics (not drawn to scale) of the symmetrically passivated monitor samples used for assessing the passivation and contact properties of a) the rear side, and b) the front side of the n-TOPCon solar cells.

Passivation properties of both surfaces were investigated by performing minority carrier lifetime (τ) measurements on the passivated regions of the respective monitors by the transient decay method, using a BT Imaging equipment. From the resulting injection level (Δn) dependent lifetime data, J_0 of the passivated regions ($J_{0,p}$) at $\Delta n = 10^{16} \text{ cm}^{-3}$ was extracted. Photoluminescence (PL) images of the monitors were also taken using the same BT Imaging equipment, revealing the passivation quality in metallized regions in terms of PL counts. Based on these counts, the findings of the lifetime measurements, and the method described in [35], J_0 of the metallized regions ($J_{0,m}$) was also determined. Furthermore, structures containing fingers with a pitch of 2 mm, and dimensions of 1 cm by $\sim 50 \mu\text{m}$ were laser-diced from the monitor samples for measuring ρ_c by the transfer length method (TLM). In the following sections, each of these parameters are reported with an extra index “r” or “f” to indicate that these belong to the rear or the front surface, respectively.

2.2 Damp Heat and Thermal Cycling Tests on 1-Cell n-TOPCon Solar Laminates

1-cell laminates of the n-TOPCon solar cells with a t_{poly} of 150 nm and polished rear surface were fabricated in a glass-glass configuration, using SmartWire Connection Technology (SWCT) foils by Meyer Burger [36], PO8110 encapsulant by 3M, and glass without ARC. To contact the wires, $\text{Sn}_{0.965}\text{Ag}_{0.035}$ -coated Cu ribbons with a width of 5 mm and a thickness of 0.3

mm were placed in contact with the SWCT foils. Subsequently, a 20 min-long lamination was performed at 150°C, while applying a pressure of 700 mbar onto the assembled structure.

The laminates were investigated both by damp heat and thermal cycling tests. For the damp heat test, a laminate was exposed to 85°C and a relative humidity of 85% for 1000 hours. Another laminate was subjected to the thermal cycling test, which took the sample repeatedly between -40°C and 85°C for 400 cycles with a cycle duration of 3 hours and a dwell time of 10 min at both temperatures. No current was applied to the laminates during thermal cycling.

The laminates were characterized by light I - V measurements under 1 sun front illumination using the LOANA system, yielding the V_{oc} , J_{sc} , FF , η , and the output power (P_{out}) of the laminates. The measurements were performed before and after the damp heat and thermal cycling tests, and in case of thermal cycling also after every 100 cycles. The evolution of P_{out} during the tests was assessed to determine whether the laminates of the n-TOPCon solar cells pass the damp heat and thermal cycling tests by exhibiting a P_{out} loss $\leq 5\%$ for a single IEC61215 test.

2.3 Roadmap for Improving the n-TOPCon Solar Cells

To establish a roadmap indicating experimental strategies to improve the efficiency of the n-TOPCon solar cells with *in situ* P-doped LPCVD-based poly-Si passivating contacts, simulations were performed using the Quokka 2 software [37]. First, a model was built to match the I - V parameters of the best solar cell with a t_{poly} of 150 nm, polished rear surface, and single ARC. The corresponding input parameters of this model are listed in Table 1. These values were selected based on experimental data, in case of e.g., $J_{0,E}$ and contact resistivity, and design parameters, in case of e.g., contact half widths, whenever available, and were otherwise chosen reasonably in order to match the I - V parameters of the best solar cell. For the input parameters not listed in Table 1, the defaults of the Quokka settings file generator were used.

Table 1. Input parameters for Quokka 2 simulations to match the best solar cell fabricated in this work with a t_{poly} of 150 nm, polished rear surface, and single ARC.

Main Parameters	Solar cell thickness: 155 μm ; Front width: 750 μm ; Rear width: 500 μm ; T : 298 K
Front Side Properties	Contact half width: 20 μm ; Emitter: 110 Ω/\square , 1 μm depth, 92% collection efficiency; Contacted region: $J_{0,E} = 632.2 \text{ fA/cm}^2$, $J_{0,2} = 0$, Contact resistivity = 2.1 $\text{m}\Omega\cdot\text{cm}^2$; Non-contacted region: $J_{0,E} = 21.3 \text{ fA/cm}^2$, $J_{0,2} = 0$

Bulk Properties	Doping type: n-type; Resistivity: 2.3 $\Omega\cdot\text{cm}$; Background lifetime: 1 ms
Rear Side Properties	Contact half width: 25 μm ; BSF: 38 Ω/\square , 150 nm depth, 0% collection efficiency; Contacted region: $J_{0,E} = 65.8 \text{ fA/cm}^2$, $J_{0,2} = 0$, Contact resistivity = 2.0 $\text{m}\Omega\cdot\text{cm}^2$; Non-contacted region: $J_{0,E} = 2.3 \text{ fA/cm}^2$, $J_{0,2} = 0$
Generation Parameters	Shading width: 13 μm (based on contact half width and geometrical calculation) Fixed Z: 12.82 (calculated with the Z calculator of PV lighthouse and using experimentally determined internal reflectance data [26,38]); Transmission: User-defined (based on measured R)
External Circuit	Series resistance: 0; Shunt resistance: $10^5 \Omega\cdot\text{cm}^2$

The remaining simulations were organized in 8 steps to establish the roadmap by improving or optimizing several solar cell parameters. These were (i) the bulk lifetime (τ_B), (ii) the bulk resistivity (ρ_B) and the contact resistivities ($\rho_{c,f}$, $\rho_{c,r}$) (iii) the screen-printed finger widths (w_f , w_r) and pitches (p_f , p_r), (iv) t_{poly} , (v) reflectance R by the use of DARC, (vi) the passivation of the non-contacted regions of the front side by the use of an advanced emitter, (vii) the passivation of the contacted regions of the front side by the use of a selective emitter, and (viii) again the front surface passivation in non-contacted regions using a transparent passivating contact. The Quokka 2 input parameters varied in each step are listed in Table 2. It is important to note that in each step the optimum values determined in preceding steps were used.

Table 2. Input parameters varied in each step of Quokka 2 simulations to improve the solar cell efficiency.

Step Number	Input Parameters
1	Bulk background lifetime: 1-8 ms
2	Bulk resistivity: 1.0-2.3 $\Omega\cdot\text{cm}$; Front and rear contact resistivity: 1.0-2.1 $\text{m}\Omega\cdot\text{cm}^2$
3	Front and rear contact half width: 10-35 μm ; Shading width: 6.5-19.5 μm ; Front unit cell width: 250-1125 μm ; Rear unit cell width: 100-700 μm
4	BSF: 38-76 Ω/\square , 150-75 nm deep; Fixed Z: 12.82-16.72
5	Transmission for DARC: Calculated with OPAL 2 (PV Lighthouse optical simulator) for 50 nm SiN_x & 90 nm SiO_x
6	Advanced emitter: 130 Ω/\square , 2 μm depth, 94% collection efficiency Front side non-contacted region: $J_{0,E} = 16 \text{ fA/cm}^2$
7	Front side contacted region: $J_{0,E} = 50\text{-}632.2 \text{ fA/cm}^2$
8	Front side non-contacted region: $J_{0,E} = 5 \text{ fA/cm}^2$

3 Performance of n-TOPCon Solar Cells and Laminates

3.1 Impact of Poly-Si Film Thickness on n-TOPCon Solar Cells

Figures of merit of the n-TOPCon solar cells with semi-textured rear surface morphology and varying t_{poly} are summarized in Table 3. While the best solar cell has an η of 22.4% along with

a relatively high FF of 81.1%, this seems to be an outlier as the best average η lies just below 22%, accompanied by significantly lower average FF values of 79.4% and below. Comparison of the average η as a function of t_{poly} shows that solar cells with thicker poly-Si films are more efficient, with a significant jump of 0.4% in η for t_{poly} increasing from 100 to 150 nm, but only a 0.1% improvement when t_{poly} is further raised to 200 nm. Differences between the other parameters of the three solar cell groups reveal two opposite trends with increasing t_{poly} , which explain the nonlinear improvement of the average η : (i) J_{sc} drops by ~ 0.15 mA/cm² per 50 nm increase in t_{poly} , and (ii) V_{oc} and FF improve, particularly when t_{poly} is raised from 100 to 150 nm.

Table 3. I - V parameters of n-TOPCon solar cells with semi-textured rear surface and varying poly-Si thicknesses in the passivating contacts at the rear. Averages and standard deviations were obtained by measurements on 8 devices per group. Parameters of the best solar cell are also shown.

t_{poly} [nm]	V_{oc} [mV]	J_{sc} [mA/cm ²]	FF [%]	η [%]	r_s [$\Omega \cdot \text{cm}^2$]	n
100	681.4 \pm 1.3	40.0 \pm 0.1	78.3 \pm 0.4	21.4 \pm 0.1	0.8 \pm 0.1	1.2 \pm 0.1
150	690.7 \pm 0.8	39.8 \pm 0.1	79.3 \pm 0.3	21.8 \pm 0.1	0.8 \pm 0.1	1.1 \pm 0.1
200	692.5 \pm 0.9	39.7 \pm 0.1	79.4 \pm 0.7	21.9 \pm 0.2	0.8 \pm 0.2	1.1 \pm 0.1
200 (Best Solar Cell)	693.7	39.7	81.1	22.4	0.5	1.1

The loss in J_{sc} with higher t_{poly} is attributed to increased parasitic absorption in the heavily doped poly-Si film, mainly due to free carrier absorption (FCA). Our previous optical studies predict a linearly increasing J_{sc} loss as a function of t_{poly} when the poly-Si passivating contact is integrated at the rear side of solar cells as in this work, with the loss equal to ~ 0.2 mA/cm² per 50 nm increase in t_{poly} [26,38]. Studies by other groups in the literature also predict similar FCA-related losses between 0.1 and 0.25 mA/cm² per 50 nm increase in t_{poly} [12,15,39]. Hence, the behavior of J_{sc} in Table 3 as a function of t_{poly} can be explained with the parasitic absorption losses reported in the literature. To verify this hypothesis, R and EQE measurements were performed, yielding the results in Fig. 3. The plot on the left shows that the solar cells with different t_{poly} have very similar optical properties at short and visible wavelengths, while R seems to decrease with increasing t_{poly} at long wavelengths, attributed to increased absorption in the poly-Si at the solar cell rear. The impact of higher t_{poly} on EQE and thus on J_{sc} is more clearly seen in the second, zoomed-in plot, which indicates a clear drop in the wavelength range of 1000 to 1200 nm. These findings agree well with the results of similar studies in the literature based on EQE measurements [15,39]. Since the optical differences are at long wavelengths i.e.,

concerned with photons reaching the rear side of the solar cells, and depend systematically on t_{poly} , the data show that FCA in the poly-Si films is indeed the reason behind the J_{sc} loss with increasing t_{poly} .

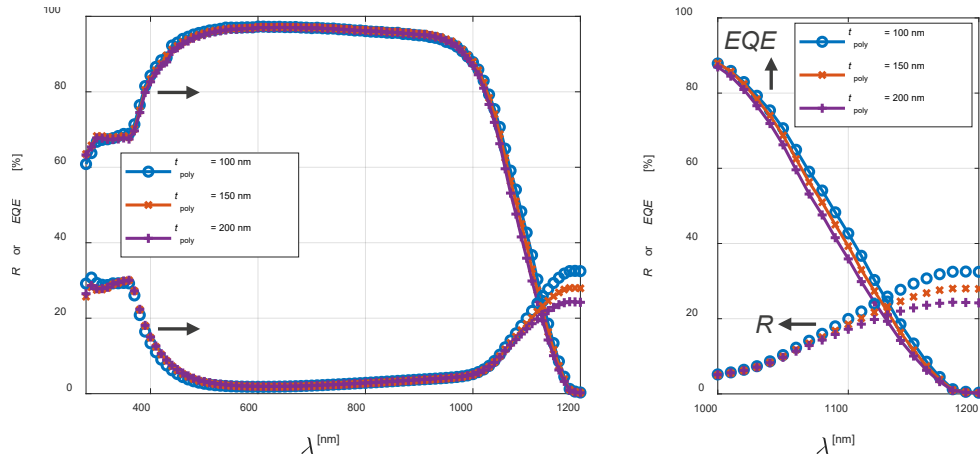


Figure 3. Reflectance (R) and external quantum efficiency (EQE) spectra of n-TOPCon solar cells with different poly-Si film thicknesses (t_{poly}). The plot on the right-hand side shows a magnified version of the first plot in the wavelength range of 1000-1200 nm.

In addition, the impact of parasitic absorption in the poly-Si films on the optical performance of solar cells is also evident from the bifaciality values of each solar cell group, measured as $82.1 \pm 0.5\%$, $80.2 \pm 0.6\%$, and $78.0 \pm 0.3\%$, for t_{poly} of 100, 150, and 200 nm, respectively. This is expected, since the parasitic absorption in the poly-Si at the illuminated side of the solar cell is known to increase with t_{poly} and also to be significantly greater than the absorption in a poly-Si film at the non-illuminated side for the same t_{poly} [40].

To understand the increasing trend of FF in Table 3 with t_{poly} , an FF loss analysis was performed, yielding the results in Fig. 4a). First, it is evident from these data that the difference between FF_n and FF i.e., the loss due to series resistance of the solar cells, is significantly larger than the difference between FF_0 and FF_n i.e., the loss due to recombination. This is expected given the relatively high r_s of $0.8 \Omega \cdot \text{cm}^2$ of the solar cells, which is attributed to issues during the screen-printing process mainly due to the use of aged Ag paste, resulting in quite regularly spaced finger interruptions at intervals of a few 100 nm as shown by the microscopy image in Fig. 4b). Poor quality of the metallization being the limiting factor for the FF is also demonstrated by the performance of the best solar cell, on which little to no finger interruptions were found. As a result, the best solar cell has a significantly lower r_s of $0.5 \Omega \cdot \text{cm}^2$ and a higher FF of 81.1%. Despite r_s -related losses being the dominant mechanism, these cannot explain

the FF trend observed, since r_s is similar for all groups of solar cells. Instead, the behavior of FF with t_{poly} seems to follow that of the FF_n . This suggests that the FF trend and particularly the $\sim 1\%$ FF improvement for a t_{poly} increase from 100 to 150 nm arise from enhanced mitigation of recombination losses, yielding a lower n value (see Table 3) and therefore an improvement in FF_n .

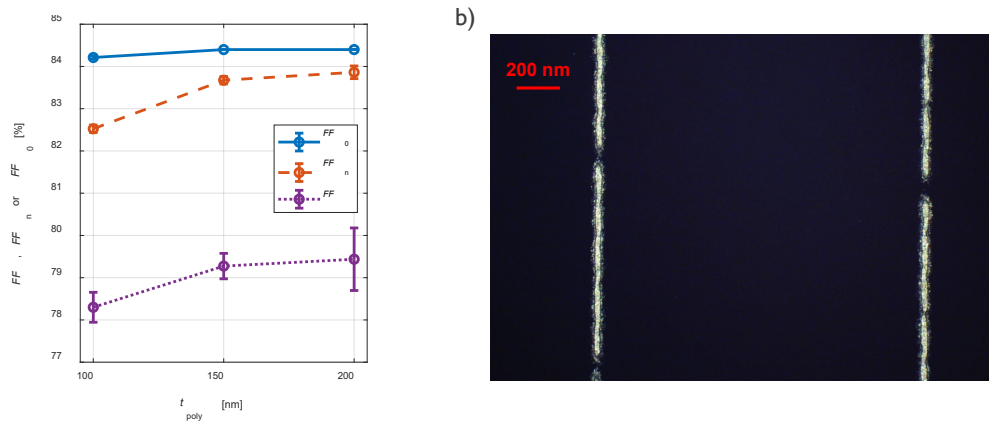


Figure 4. a) Fill factor (FF) of the n-TOPCon solar cells with different t_{poly} , together with the FF without the impact of the series resistance (FF_n), as well as the FF without the impact of both the series resistance and the non-unity ideality factor (FF_0). b) Optical microscopy image of a solar cell fabricated during the t_{poly} screening experiment, showing the quite regularly and closely spaced interruptions in screen-printed fingers.

The positive impact of using a t_{poly} of 150 nm or higher in mitigating recombination losses was verified by characterizing the symmetrically passivated monitors. The results, depicted in Fig. 5a), show that $J_{0,m,r}$ decreases by more than a factor of 5, to values below 100 fA/cm², when t_{poly} is increased from 100 to 150 nm, showing that passivating contacts with thicker poly-Si films preserve their carrier selectivity better against aggressive screen-printed metallization. This observation agrees with the findings of similar studies in the literature [14,15,41–43]. Moreover, according to Fig. 5a), $J_{0,p,r}$ decreases slightly, to 3.6 fA/cm², for higher t_{poly} , which agrees with the trend reported in some works in the literature [14,15], while other works did not identify any trend in $J_{0,p,r}$ as a function of t_{poly} [41,43]. Overall, the reduction in $J_{0,m,r}$ and $J_{0,p,r}$ with increasing t_{poly} indicate that the use of thicker poly-Si films lead to lower recombination losses. Both the $\sim 1\%$ higher FF_n and FF , and the ~ 10 mV higher V_{oc} for $t_{\text{poly}} \geq 150$ nm are attributed to enhanced mitigation of recombination in case of thicker poly-Si. Another benefit of using higher t_{poly} is the achievement of lower $\rho_{c,r}$, down to 1.7 m Ω ·cm², as Fig. 5b) shows. As for $J_{0,p,r}$, the decrease in $\rho_{c,r}$ with increasing t_{poly} agrees with some [14,15,43], but not all results in the literature [41]. Comparison of all these findings regarding the impact of t_{poly} on poly-Si passivating contact properties, obtained here on semi-textured

surfaces, with the corresponding results on textured surfaces reported in our previous work indicate a good agreement [26]. Despite the reproducibility of the results, it is not well-understood why $J_{0,p,r}$ and $\rho_{c,r}$ are lower for higher t_{poly} . This calls for a more detailed study on the impact of t_{poly} on the poly-Si film properties such as the doping profile, which is beyond the scope of this work and will be targeted in the future.

In addition to the properties of the passivating contact at the rear, Fig. 5 reveals for the front surface that a low $\rho_{c,f} = 2.1 \text{ m}\Omega\cdot\text{cm}^2$ can be achieved, but with a poor passivation quality as indicated by the high $J_{0,p,f} = 21.3 \text{ fA/cm}^2$ and $J_{0,m,f} = 632.2 \text{ fA/cm}^2$. This is expected given the lack of passivating contacts at the front side and appears to be the main factor limiting the V_{oc} of the solar cells. This finding agrees with the results of similar recombination loss analyses reported in the literature for n-TOPCon solar cells [5,16].

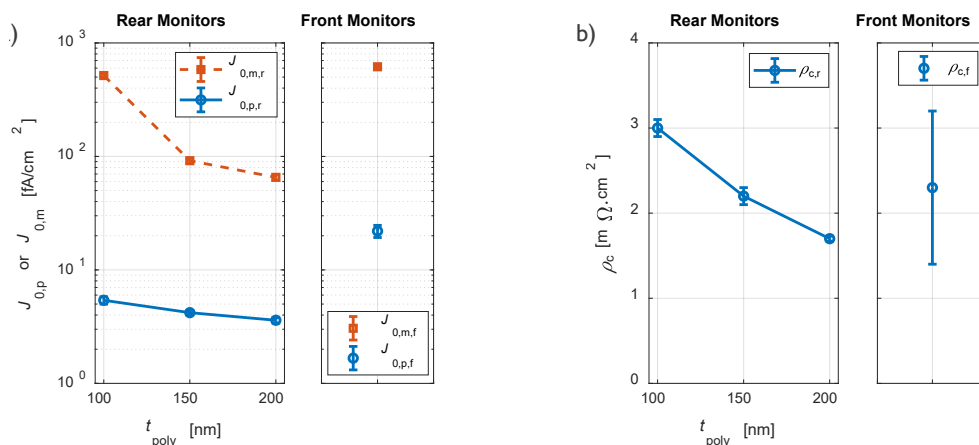


Figure 5. a) Recombination current density in passivated ($J_{0,p}$) and in screen-printed ($J_{0,m}$) regions of rear monitors (index “r”) as a function of the poly-Si thickness (t_{poly}), and of the front monitors (index “f”). b) Contact resistivity (ρ_c) of rear monitors (index “r”) as a function of t_{poly} and of front monitors (index “f”).

Overall, these results show that a thick enough poly-Si film with $t_{\text{poly}} \geq 150 \text{ nm}$ is necessary to achieve high-quality passivating contacts and high-efficiency n-TOPCon solar cells for the screen-printed contacts used. While choosing $t_{\text{poly}} > 150 \text{ nm}$ results in slightly improved electrical properties of the devices, it also leads to optical losses, showing only marginal improvements in terms of η . It is expected that, for t_{poly} beyond 200 nm, η might drop due to increased J_{sc} losses, which might limit the solar cell performance, as shown in the literature [15]. For these reasons, 150 nm was chosen as the poly-Si thickness for the rear surface morphology screening experiment in this work. Apart from the choice of a sufficiently high t_{poly} , it is evident that improving the screen-printing process to avoid finger interruptions and

thus increase the FF can offer significant gains in η . Therefore, new bottles of screen-printing pastes and new screens adapted to the wafer size were used for the rear surface morphology screening experiment.

3.2 Impact of Rear Surface Morphology on n-TOPCon Solar Cells

For studying the impact of the rear surface morphology on the solar cell characteristics, n-TOPCon solar cells with semi-textured and polished rear surfaces were prepared. The morphologies of a fully textured surface as a reference, and the semi-textured and the polished surfaces are illustrated in the SEM images shown in Fig. 6a), 6b), and 6c) respectively. Findings of the I - V characterization of n-TOPCon solar cells with $t_{\text{poly}} = 150$ nm and the semi-textured and polished rear surface morphologies are shown in Table 4. First, comparison of the semi-textured reference group with the corresponding results in Table 3 for $t_{\text{poly}} = 150$ nm shows that the average η has slightly improved by 0.1%. This is due to the 0.7% jump in FF , which follows from the lower r_s of $0.6 \Omega \cdot \text{cm}^2$, and is attributed to the improved screen-printing process, yielding little to no finger interruptions as found by optical microscopy. The reason for the limited gain in η despite this significant FF increase seems to be the drop in V_{oc} by 2.4 mV. To understand this loss in V_{oc} , PL images of monitor samples from the t_{poly} screening and rear surface morphology screening experiments were compared. The design of the monitors with regions of different metallization fractions (MF) is depicted in Fig. 7a). As shown in Fig. 7b), the non-metallized regions of the monitor from the t_{poly} screening experiment are uniformly passivated, while the monitor from the rear surface morphology screening experiment, depicted in Fig. 7c), has lower PL counts i.e., darker regions at the edges. This is attributed to unexpected contamination of the edges, found to be originating from the boat of the PECVD equipment used. By contrast, the darker color in the metallized regions is expected due to elevated recombination because of metallization, which clearly increases with higher MF in Fig. 7b) and 7c).

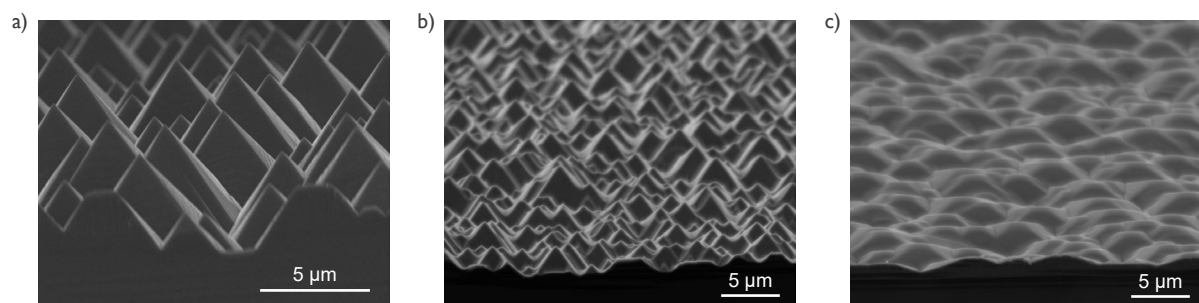


Figure 6. Scanning electron microscopy (SEM) images of a) a fully textured, b) the semi-textured and c) the polished rear surface morphology.

Table 4. I - V parameters of n-TOPCon solar cells with 150 nm thick poly-Si in the passivating contact at the rear and different rear surface morphologies. Averages and standard deviations were obtained by measurements on 7-14 devices per group. Parameters of the best solar cell are also shown.

Rear Surface	V_{oc} [mV]	J_{sc} [mA/cm ²]	FF [%]	η [%]	r_s [$\Omega \cdot \text{cm}^2$]	n
Semi-textured	688.3±0.8	39.8±0.1	80.0±0.5	21.9±0.2	0.6±0.1	1.1±0.1
Polished	689.5±1.1	40.3±0.1	80.2±0.3	22.3±0.1	0.6±0.1	1.1±0.1
Polished (Best Solar Cell)	690.2	40.4	80.4	22.4	0.6	1.1

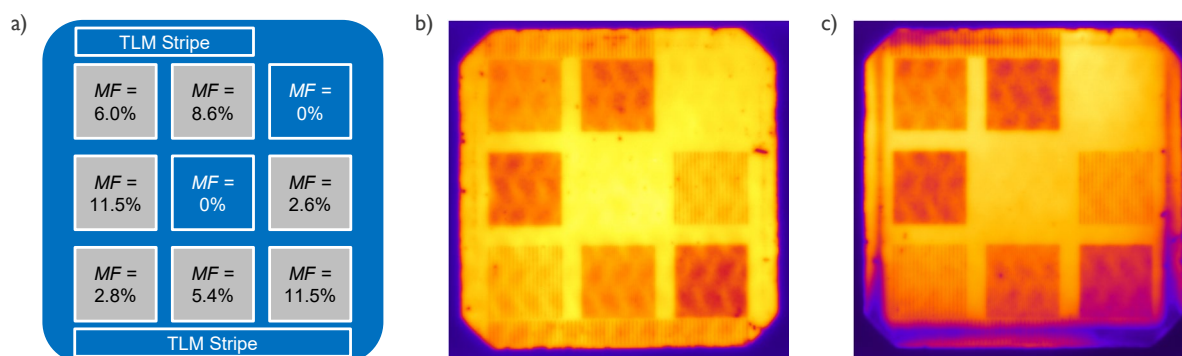


Figure 7. a) Schematic of the symmetrically passivated monitors investigated by photoluminescence (PL) imaging. The metallization fraction (MF) in each square on the monitors is indicated. b,c) PL images of the monitors with semi-textured surface morphology and poly-Si thickness of 150 nm from b) the t_{poly} screening experiment and c) the rear surface morphology screening experiment. The regions with poorer passivation and lower PL counts appear darker in the images.

Table 4 also reveals that the flatter rear surface morphology resulting from polishing allows the fabrication of n-TOPCon solar cells which are 0.4% more efficient on average. While minor improvements are observed in V_{oc} and FF of the solar cells with polished rear, the main reason behind the efficiency gain is clearly the 0.5 mA/cm² increase in J_{sc} . Results of R and EQE measurements performed on solar cells with different rear surface morphology, depicted in Fig. 8a), reveal that the optical improvement originates from a gain in EQE at long wavelengths. This leads to the conclusion that the polished rear surface offers enhanced light trapping compared to the semi-textured one, which also explains the higher R at long wavelengths, as more light is internally reflected at the polished rear, increasing the escape reflectance. It is important to note, however, that the use of the polished rear surface also reduces the bifaciality from 81.2±0.3% in the case of the semi-textured rear, to 78.7±0.5%. This is because of the J_{sc} under rear illumination decreasing by 0.8 mA/cm² due to an increased R in the case of the polished rear surface. The impact of this drop in bifaciality on the energy yield at the PV system level requires further investigation, which is beyond the scope of this work.

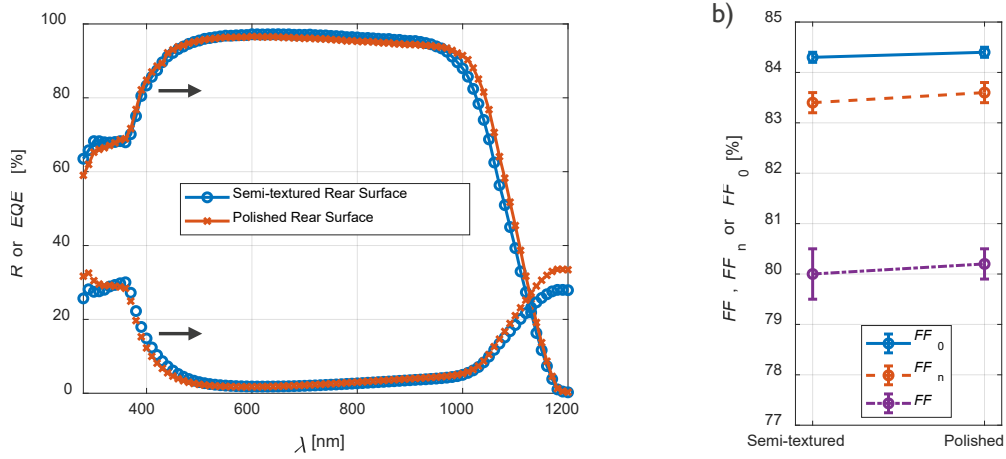


Figure 8. a) Reflectance (R) and external quantum efficiency (EQE) spectra of n-TOPCon solar cells with different rear surface morphologies. b) Fill factor (FF) of the n-TOPCon solar cells with different rear surface, together with the FF without the impact of the series resistance (FF_n), as well as the FF without the impact of both the series resistance and the non-unity ideality factor (FF_0).

Concerning the impact of rear surface morphology on the FF , the analysis in Fig. 8b) shows that the dominant loss mechanism remains r_s -related for both morphologies as in Fig. 4a), albeit with a lower drop from FF_n to FF than in the t_{poly} screening experiment, given the lower r_s in Table 4 than in Table 3. Furthermore, the minor improvement in FF for the solar cells with polished rear follows from the increase in FF_n by the same margin of 0.2% i.e., from enhanced mitigation of recombination losses. This conclusion is supported by the $\sim 45\%$ lower $J_{0,p,r}$ of 2.3 fA/cm² and $J_{0,m,r}$ of 65.8 fA/cm² found for the polished monitors, as depicted in Fig. 9a). This finding agrees with the results in the literature [5]. The observed reduction in recombination losses also explains the 1.2 mV increase in V_{oc} of the solar cells with polished rear surface. Achievement of lower $J_{0,p,r}$ and $J_{0,m,r}$ on the flatter polished surface is attributed to three factors based on the literature: (i) the reduced surface area compared to the semi-textured surface, (ii) the lower dangling bond density of (100)-oriented surfaces than the (111)-oriented facets, with the former and the latter exposed to a greater extent in case of the polished and semi-textured surfaces, respectively, and (iii) the reduction in stress related defects in the SiO_x film [44]. Moreover, Fig. 9b) shows that $\rho_{c,r}$ decreases from 2.5 m Ω ·cm² in case of the semi-textured surface to 2.0 m Ω ·cm² when the surface is polished, which is surprising as a higher contact resistivity would be expected due to the lower contact area. The reason behind this $\rho_{c,r}$ reduction is not well-understood and given the relatively high standard deviation of 0.3 m Ω ·cm² of the $\rho_{c,r}$ data in case of the polished surface, the observed drop should be treated with caution and might be inconclusive.

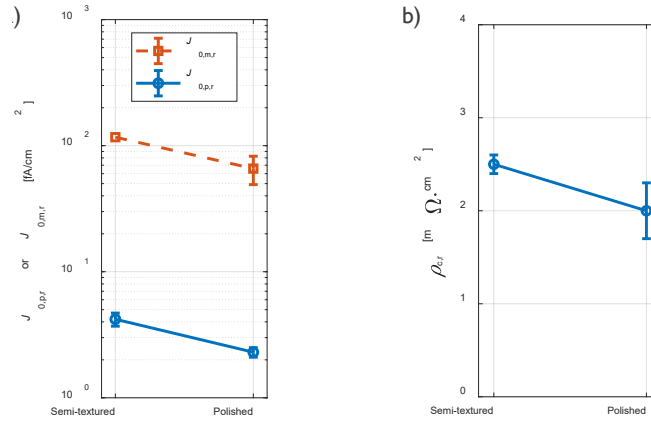


Figure 9. a) Recombination current density in passivated ($J_{0,p,r}$) and in screen-printed ($J_{0,m,r}$) regions of rear monitors with different surface morphology. b) Contact resistivity of the rear monitors ($\rho_{c,r}$) with different surface morphology.

The findings of the solar cell development thus reveal that the use of a sufficiently thick poly-Si film and a polished rear surface morphology are key for enabling high efficiencies. For further increasing the η , two strategies seem plausible: (i) reducing the total J_0 and thus improving the V_{oc} of the devices by enhancing the passivation of the front surface and by passivating the front contacts as the high $J_{0,p,f}$ and $J_{0,m,f}$ in Fig. 5 suggest, and (ii) improving the relatively low EQE of the devices at short wavelengths, as Fig. 8a) shows. While the former is challenging to achieve with industrial processes, the latter is feasible by realizing a DARC at the front surface, which was chosen as the final step of improvement in this work.

3.3 Impact of Using DARC on n-TOPCon Solar Cells

Table 5 shows the improvement achieved by using the DARC consisting of a stack of 70 nm SiN_x and 90 nm SiO_x films on four of the best solar cells with polished rear surface. First, the best solar cell with a certified η of 23.01% and a high V_{oc} of 691.7 mV (see Fig. 10), fabricated with the industrial process in Fig. 1b), clearly demonstrates the potential of passivating contacts with *in situ* P-doped poly-Si films deposited by LPCVD. This result matches the highest η obtained in the literature with a large-area n-TOPCon solar cell incorporating an *in situ* doped LPCVD-based poly-Si passivating contact [25]. Moreover, the achieved η is also on par with the highest certified η of 23.06% obtained in our group using the conventional *ex situ* doped LPCVD-based poly-Si passivating contacts (data not published yet). Second, it is important to note that the certified FF of the best solar cell is 1.1% higher than the corresponding FF measured in-house, which is attributed to the certified measurement neglecting front and rear grid-resistance contributions, as indicated in Fig. 10 [45]. Nevertheless, even with 1.1% higher

FF , resistive losses remain dominant and the discussions in previous sections regarding the FF loss analyses are valid. Third, DARC yields an average increase in η by 0.2%, which is due to a significant improvement in J_{sc} by 0.5 mA/cm². The resulting average J_{sc} of 40.8 mA/cm² matches the J_{sc} obtained in the literature using a similar DARC design on n-TOPCon solar cells [33]. We would like to note that using a DARC at the rear side of the solar cells can also be useful for boosting the bifaciality, but this would come at the price of increased process complexity. Table 5 also shows that, as expected, DARC has little to no impact on V_{oc} . The FF does not show a significant change either, only a 0.2% drop, and the r_s does not change, even though the extra SiO_x film to realize the DARC was deposited onto the Ag fingers. We speculate that the wires of the I - V measurement setup with high mechanical tension punch through the thin SiO_x film on the Ag fingers and the realization of the DARC on the finished solar cells therefore does not lead to contacting issues.

Table 5. I - V parameters of n-TOPCon solar cells with single and double antireflection coating (ARC). Averages and standard deviations were obtained by measurements on 4 devices with 150 nm thick poly-Si in the passivating contact at the rear and with the polished rear surface morphology. Parameters of the best solar cell determined by certified measurements at ISFH CalTeC are also shown.

Front ARC	V_{oc} [mV]	J_{sc} [mA/cm ²]	FF [%]	η [%]	r_s [$\Omega \cdot \text{cm}^2$]	n
Single ARC	690.5±0.3	40.3±0.1	80.3±0.1	22.4±0.1	0.6±0.1	1.1±0.1
Double ARC	690.6±0.5	40.8±0.1	80.1±0.2	22.6±0.1	0.6±0.1	1.1±0.1
Double ARC (Best Solar Cell – Calibrated Measurement)	691.7	40.95	81.25	23.01	-	-

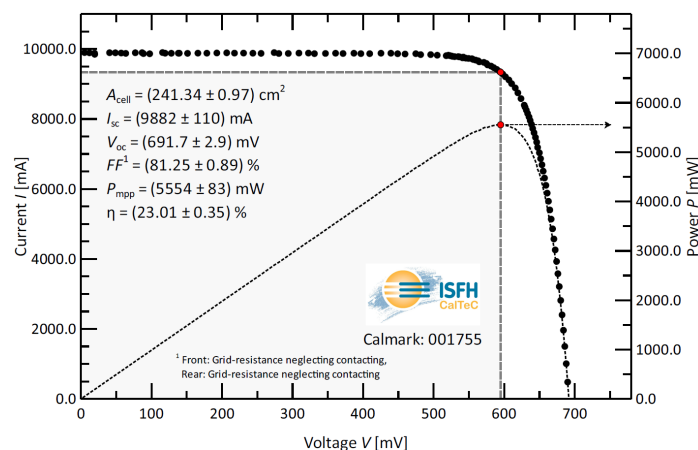


Figure 10. Result of the certified I - V measurement of the best n-TOPCon solar cell fabricated in this work.

Further analysis of the J_{sc} increase after the realization of the DARC was performed by R and EQE measurements on solar cells with single and double ARC, as shown in Fig. 11. It is evident

from these data that the reduced R at short and long wavelengths and the resulting increase in EQE cause the optical improvement of the solar cells, as expected. It is important to note that the thickness of the SiN_x film in the DARC structure was optimized for a single but not double ARC, yielding the second dip in R at a quite long wavelength of ~ 1000 nm. Hence, room for further improvement of the R spectrum, the J_{sc} , and thus the η exists by optimizing the DARC stack.

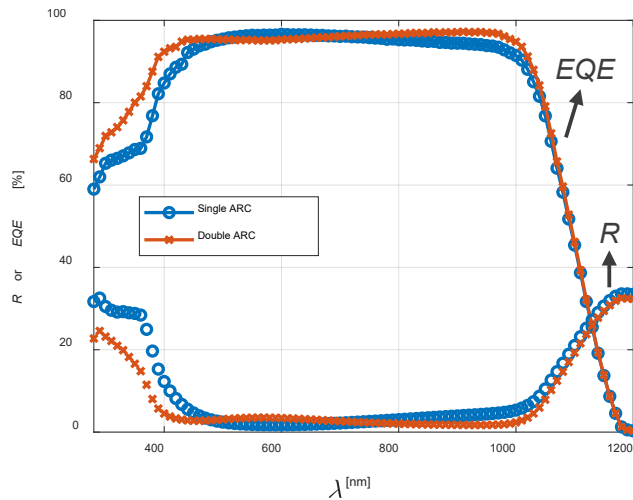


Figure 11. Reflectance (R) and external quantum efficiency (EQE) spectra of n-TOPCon solar cells with single and double antireflection coating (ARC).

3.4 Damp Heat and Thermal Cycling Tests on 1-Cell n-TOPCon Solar Laminates

The results of the damp heat and thermal cycling tests applied to 1-cell laminates containing the developed n-TOPCon solar cells are shown in Fig. 12. These indicate that P_{out} of the laminates, initially equal to ~ 4.9 W, does not drop and even increase by $\sim 1\%$ relative upon 1000 h of damp heat testing (see Fig. 12a)) and by $\sim 2\%$ relative after 400 thermal cycles (see Fig. 12b)). Hence, the laminates pass the damp heat and thermal cycling tests (P_{out} loss $\leq 5\%$ for a single IEC61215 test), showing that the screen-printed fingers of the developed solar cells do not degrade due to moisture and the interconnections between the fingers and the wires of the laminates do not fail due to thermal cycling. The results of this first assessment indicate that the developed solar cells can be suitable for integration in PV modules in the glass-glass configuration. In the more conventional glass-backsheet configuration, PV modules are known to be more susceptible to failure, particularly during the damp heat test, due to moisture ingress through the backsheet [46]. Hence, for assessing the suitability of the developed solar cells for application in glass-backsheet modules, the applied tests are to be repeated using the glass-backsheet configuration. Furthermore, for a complete study of the reliability of PV modules

based on the developed n-TOPCon solar cells, further investigations such as potential induced degradation and humidity freeze tests are required and will be performed in the future.

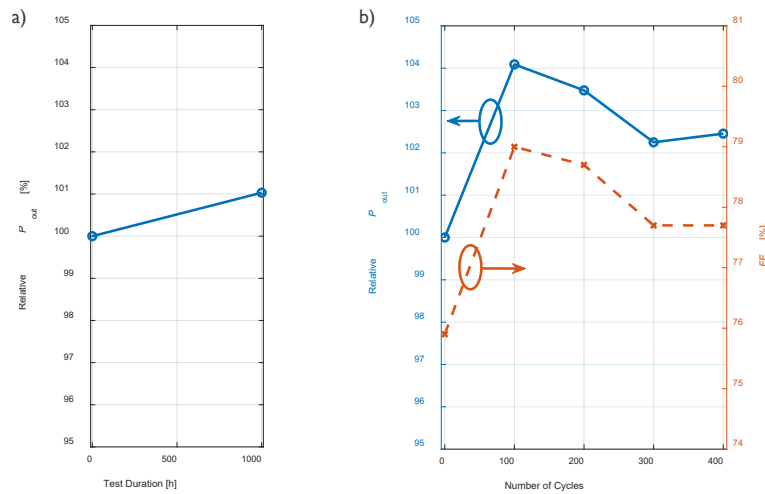


Figure 12. a) The relative output power (P_{out}) of the laminate subjected to the damp heat test, before and after 1000 hours of testing. b) Evolution of the relative P_{out} and the fill factor (FF) of the laminate subjected to thermal cycling, as a function of the number of cycles.

Further analysis of the $I-V$ parameters of the laminates leads to a few more conclusions. First, for both laminates, the cell-to-laminate losses were found to be high, with the laminates having $\sim 2\%$ absolute lower η than the cells, equal to 20.1-20.3%. This is expected, as the laminates were not optimized for maximizing the η . Among the other $I-V$ parameters, the V_{oc} does not change significantly upon lamination, remaining at ~ 690 mV, while the J_{sc} drops by ~ 1.6 mA/cm², to ~ 38.7 mA/cm², because of the optical losses at laminate level, mainly due to the use of glass without ARC for the preparation of the laminates. Moreover, the FF drops by $\sim 4.5\%$ absolute, to 75.5-75.9%, which is attributed to the series resistance contribution of the interconnections, raising the r_s of the laminates to ~ 1.5 $\Omega \cdot \text{cm}^2$, which is significantly higher than the r_s of the solar cells before lamination. Investigating the impact of the performed tests on the $I-V$ parameters of the laminates shows that, for the laminate subjected to the damp heat test, the 1% relative increase in P_{out} originates mainly from an increase in J_{sc} , from 38.7 mA/cm² to 39 mA/cm². This improvement in J_{sc} is not well-understood. For the thermal cycling, the evolution of P_{out} clearly follows the FF of the laminate, as depicted in Fig. 12b). Other $I-V$ parameters were found to remain unchanged during thermal cycling. Interestingly, FF increased significantly, by 3.1% absolute, during the first 100 cycles, after which it dropped by 1.3% absolute during the following 300 cycles. The initial FF improvement is associated with a significant drop in the series resistance of the laminate, which is attributed to modifications in the properties of the interconnections, as the series resistance of the solar cell

itself is not expected to change during thermal cycling. Nevertheless, the physical mechanism behind the change in the properties of the interconnections is not well-understood.

4 Roadmap for Improving the n-TOPCon Solar Cells

While a high certified η of 23.01% is demonstrated in this work, it is important to assess the ultimate potential of the n-TOPCon solar cells with *in situ* P-doped LPCVD poly-Si passivating contacts, as record large-area n-TOPCon solar cells fabricated by the PV industry already achieved η up to 25.4% [4]. For this purpose, a roadmap is established by Quokka 2 simulations and presented in Fig. 13, showing that, with proper design and process optimizations, solar cells with η of 25.5% can be achieved using *in situ* P-doped LPCVD poly-Si passivating contacts.

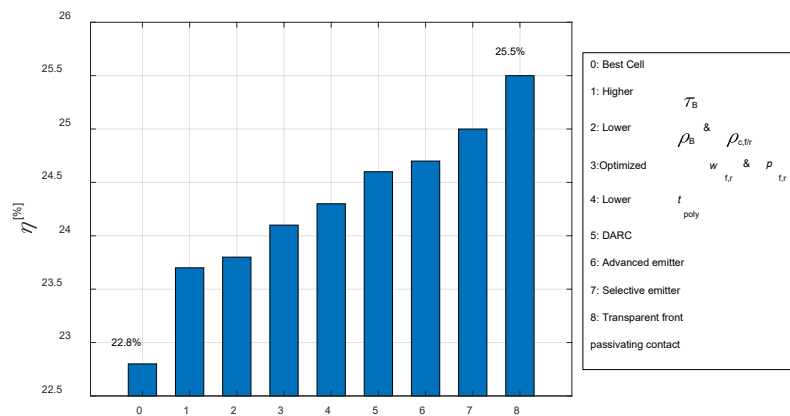


Figure 13. Roadmap to 25.5% n-TOPCon solar cell efficiency established by Quokka 2 simulations. The improvements to the solar cell design and fabrication process applied in each simulation step are listed at the right-hand side.

Figure 13 shows that the initial simulation to match the best solar cell using the parameters in Table 1 yields $\eta = 22.8\%$, along with $V_{oc} = 694.7$ mV, $J_{sc} = 40.4$ mA/cm², and $FF = 81.1\%$. Comparison of these simulation results with the measured I - V parameters in Table 4 of the modeled best solar cell indicate 0.4% higher simulated η due to 0.7% higher simulated FF and 4.5 mV higher simulated V_{oc} , while the simulated and the measured J_{sc} are perfectly matched. This is expected, since (i) accurately measuring the FF of zero-busbar devices is difficult and the measured FF can be an underestimation, particularly given the 1.1% difference between the FF determined in-house and at ISFH CalTeC as discussed in Section 3.3, and (ii) the V_{oc} of the best solar cell suffered a 2-3 mV loss due to the contamination at the edges as discussed in Section 3.2, which is not considered in the simulations. Therefore, the model of the best solar cell based on the parameters in Table 1 is considered valid.

The main factors limiting the efficiency of the best solar cell were found to be recombination losses in the bulk and at the front surface and contacts. As wafers with significantly higher bulk quality i.e., τ_B up to 8 ms are commercially available [47], the first step of the roadmap assessed the improvement achievable by improving the wafer quality. As Fig. 13 shows, the use of wafers with $\tau_B = 8$ ms leads to a significant η gain of 0.9% due to the FF and the V_{oc} increasing by 1.9% and 9 mV, respectively. It is interesting to note that most of this gain (0.7% in η) can be obtained already for $\tau_B = 4$ ms, showing that the increase in η with τ_B has a saturating behavior. Step 2 and 3 of the roadmap shows that η can then be increased by 0.4%, to above 24%, by (i) reducing ρ_B to 1 $\Omega \cdot \text{cm}$, and $\rho_{c,f}$ and $\rho_{c,r}$ to 1 $\text{m}\Omega \cdot \text{cm}^2$ using improved screen-printing pastes, (ii) further developing the screen-printing process to realize narrower fingers with $w_f = w_r = 20 \mu\text{m}$, and (iii) optimizing the grid design for the lower $\rho_{c,f}$ and $\rho_{c,r}$ by increasing the pitch of the fingers. These improvements mainly affect the FF , yielding a 0.6% increase. In step 4, another η gain of 0.2% is predicted when going for thinner poly-Si films with $t_{\text{poly}} = 75$ nm, which is expected to become the industry standard thickness by 2028 when new screen-printing pastes which can contact thinner poly-Si films with low $J_{0,m}$ are developed [1]. As explained before, reduced t_{poly} results in less FCA and a consequent 0.3 mA/cm^2 increase in J_{sc} . An impressive η of 24.3% i.e., a gain of 1.5% absolute, can be achieved after these 4 steps of the roadmap, relying on industrially feasible improvements only.

In step 5, implementing a DARC enhances the J_{sc} and the η by 0.6 mA/cm^2 and 0.3%, respectively, in agreement with the experimental results in Table 5. It should be noted, however, that this improvement would not translate to module level due to optical losses in encapsulants and as the refractive index of the SiO_x film used in the simulations as the top layer of DARC is not suitable for module applications. Lastly, steps 6, 7, and 8 of the roadmap foresee the reduction in recombination losses at the front surface of the solar cell. In step 6, the losses in the non-metallized regions are decreased using a deeper, advanced emitter. The advanced emitter is known to yield a lower $J_{0,p,f}$ of 16 fA/cm^2 [48], and results in 3 mV higher V_{oc} and 0.1% higher η . In step 7, recombination losses in the metallized regions are reduced by introducing a selective emitter. The selective emitter is assumed to reduce $J_{0,m,f}$ down to 50 fA/cm^2 , a value possibly achievable with p-type passivating contacts, yielding 7 mV higher V_{oc} and 0.3% higher η , thus reaching $\eta = 25\%$. While the improvements to the emitter considered in steps 6 and 7 are available technologies and can be used for fabricating solar cells with record efficiencies, it can be difficult to implement those in production, since fabrication of the advanced emitter requires a long process duration [48] and realizing the selective emitter

requires patterning, increasing the process complexity. In step 8, recombination losses in the non-metallized regions of the front surface are further reduced using a transparent passivating contact at the front, covering the entire solar cell. This could potentially be achieved by applying a full-area p-type poly-Si passivating contact to the front surface and thinning down the poly-Si film between the contact fingers to obtain low thicknesses and mitigate parasitic absorption losses [49,50]. For the transparent passivating contact, a $J_{0,p,r}$ of 5 fA/cm² is assumed in step 8. This yields an 11 mV increase in V_{oc} , a 0.3% improvement in FF , and a 0.5% higher η , resulting in $\eta = 25.5\%$.

5 Summary and Outlook

Realizing *in situ* P-doped poly-Si films by LPCVD offers the prospect of simplifying the manufacturing of industrial n-TOPCon solar cells, by eliminating the need for an external doping process, prevalent in the industry today. In this work, the potential of *in situ* P-doped LPCVD poly-Si films was demonstrated at solar cell and laminate level, by integrating them in passivating contacts at the rear side of large-area bifacial n-TOPCon devices. To achieve the highest efficiencies possible, the solar cell design was optimized starting with an investigation on the impact of the poly-Si film thickness on the solar cell performance. This study revealed the necessity of using a $t_{poly} \geq 150$ nm to properly passivate the areas metallized by screen-printing, allowing $J_{0,m,r} < 100$ fA/cm². While such thicker layers were found to yield slightly lower $J_{0,p,r}$ and $\rho_{c,r}$ as well, they were also responsible for increased FCA, reducing the J_{sc} of the solar cells by ~ 0.15 mA/cm² per 50 nm increase in t_{poly} . As a result of this trade-off between the electrical and optical properties of the devices, the average η saturated just below 22% for $t_{poly} \geq 150$ nm, when a semi-textured rear surface morphology was used. A t_{poly} of 150 nm was therefore chosen for further development.

Further improvement of the solar cell design was achieved by realizing a flatter, polished rear surface for the devices, resulting in an average η of 22.4%. This was found to be mainly due to improved light trapping at the rear side, increasing J_{sc} by 0.5 mA/cm². The electrical performance of the passivating contact also improved on the polished surface, yielding $J_{0,p,r} = 2.3$ fA/cm², $J_{0,m,r} = 65.8$ fA/cm², and $\rho_{c,r} = 2.0$ m Ω ·cm². A further gain in J_{sc} by 0.5 mA/cm² was then obtained by applying a double ARC to the front surface of the devices, in the form of an additional SiO_x layer on top of the SiN_x layer, which resulted in a broadband reduction in R . This resulted in η being higher by 0.2% on average, and the best solar cell had a calibrated η of 23.01%, accompanied by a high V_{oc} of 691.7 mV, and a high J_{sc} of 40.95 mA/cm².

The fabricated n-TOPCon solar cells were also incorporated in 1-cell laminates, which were subjected to 1000 h of damp heat testing and 400 cycles of thermal cycling. Upon both tests, P_{out} of the laminates did not degrade but increased by 1-2%. Hence, the laminates passed the tests, indicating that the developed solar cells can be suitable for use in PV modules.

Lastly, the ultimate efficiency potential of n-TOPCon solar cells with *in situ* P-doped LPCVD poly-Si passivating contacts was predicted by establishing a roadmap to an η of 25.5% using Quokka 2 simulations. Among the strategies outlined in the roadmap, the most effective improvements to the solar cell design and fabrication process were found to be the use of wafers with higher bulk lifetimes and of advanced and selective emitter as well as transparent passivating contact technologies for enhanced passivation of the front side of the solar cells.

Our future work will focus on following the roadmap established in this paper to achieve the foreseen improvements to η experimentally. Furthermore, further simplification of the process used for fabricating n-TOPCon solar cells will be targeted by developing fired passivating contacts based on the *in situ* P-doped LPCVD poly-Si films used in this work, thereby skipping the post-LPCVD annealing process.

Acknowledgments

The authors would like to acknowledge Sukhvinder Singh from Imec and Rajiv Sharma from KU Leuven for the valuable discussions and their help with the sample fabrication.

This work was supported by the European Union's Horizon2020 Programme for research, technological development, and demonstration [grant number 857793]; and by the Kuwait Foundation for the Advancement of Sciences [grant number CN18-15EE-01].

References

- [1] M. Fischer, M. Woodhouse, S. Herritsch, J. Trube, International Technology Roadmap for Photovoltaic 2020 Results, 2021.
- [2] D. Yan, A. Cuevas, J.I. Michel, C. Zhang, Y. Wan, X. Zhang, J. Bullock, Polysilicon passivated junctions: The next technology for silicon solar cells?, *Joule*. 5 (2021) 811–828. <https://doi.org/10.1016/j.joule.2021.02.013>.
- [3] A. Richter, R. Müller, J. Benick, F. Feldmann, B. Steinhauser, C. Reichel, A. Fell, M.

- Bivour, M. Hermle, S.W. Glunz, Design rules for high-efficiency both-sides-contacted silicon solar cells with balanced charge carrier transport and recombination losses, *Nat. Energy*. 6 (2021) 429–438. <https://doi.org/10.1038/s41560-021-00805-w>.
- [4] L. Stoker, JinkoSolar claims new record taking n-type cell conversion efficiency to 25.4% - *PV Tech*, (2021). <https://www.pv-tech.org/jinkosolar-claims-new-record-taking-n-type-cell-conversion-efficiency-to-25-4/> (accessed November 12, 2021).
- [5] D. Chen, Y. Chen, Z. Wang, J. Gong, C. Liu, Y. Zou, Y. He, Y. Wang, L. Yuan, W. Lin, R. Xia, L. Yin, X. Zhang, G. Xu, Y. Yang, H. Shen, Z. Feng, P.P. Altermatt, P.J. Verlinden, 24.58% total area efficiency of screen-printed, large area industrial silicon solar cells with the tunnel oxide passivated contacts (i-TOPCon) design, *Sol. Energy Mater. Sol. Cells*. 206 (2020). <https://doi.org/10.1016/j.solmat.2019.110258>.
- [6] Y. Chen, D. Chen, P.P. Altermatt, G. Xu, Z. Wang, C. Liu, Y. Zou, Y. He, Y. Wang, J. Gong, L. Yuan, W. Liu, Y. Chen, M. Deng, Y. Hu, S. Chen, J. Xiang, H. Shen, S. Zhang, L. Wang, X. Zhang, Y. Yang, Z. Feng, P.J. Verlinden, >25% LARGE-AREA INDUSTRIAL SILICON SOLAR CELL: LEARNING FROM HISTORY AND FUTURE PERSPECTIVE, in: *Proc. 36th Eur. Photovolt. Sol. Energy Conf. Exhib.*, 2019: pp. 294–299. <https://doi.org/10.4229/EUPVSEC20192019-2EO.1.2>.
- [7] C. Xiao, Taking TopCON to Top Runner: Jolywood president Lin Jianwei talks solar n-type cell innovation - *PV Tech*, (2020). <https://www.pv-tech.org/taking-topcon-to-top-runner-jolywood-president-lin-jianwei-talks-solar-n-type-cell-innovation/> (accessed July 15, 2021).
- [8] R. Chen, P. Zheng, M. Wright, D. Chen, J. Yang, A. Ciesla, S. Wenham, 24.58% efficient commercial n-type silicon solar cells with hydrogenation, *Prog. Photovoltaics Res. Appl.* (2021) 1–6. <https://doi.org/10.1002/pip.3464>.
- [9] J. Schmidt, R. Peibst, R. Brendel, Surface passivation of crystalline silicon solar cells: Present and future, *Sol. Energy Mater. Sol. Cells*. 187 (2018) 39–54. <https://doi.org/10.1016/j.solmat.2018.06.047>.
- [10] M. Hermle, F. Feldmann, M. Bivour, J.C. Goldschmidt, S.W. Glunz, Passivating contacts and tandem concepts: Approaches for the highest silicon-based solar cell efficiencies, *Appl. Phys. Rev.* 7 (2020). <https://doi.org/10.1063/1.5139202>.
- [11] Y. Chen, D. Chen, C. Liu, Z. Wang, Y. Zou, Y. He, Y. Wang, L. Yuan, J. Gong, W. Lin, X. Zhang, Y. Yang, H. Shen, Z. Feng, P.P. Altermatt, P.J. Verlinden, Mass production of industrial tunnel oxide passivated contacts (i-TOPCon) silicon solar cells with average efficiency over 23% and modules over 345 W, *Prog. Photovoltaics Res.*

- Appl. 27 (2019) 827–834. <https://doi.org/10.1002/pip.3180>.
- [12] M.K. Stodolny, M. Lenes, Y. Wu, G.J.M. Janssen, I.G. Romijn, J.R.M. Luchies, L.J. Geerligns, n-Type polysilicon passivating contact for industrial bifacial n-type solar cells, *Sol. Energy Mater. Sol. Cells*. 158 (2016) 24–28. <https://doi.org/10.1016/j.solmat.2016.06.034>.
- [13] M.K. Stodolny, J. Anker, B.L.J. Geerligns, G.J.M. Janssen, B.W.H. Van De Loo, J. Melskens, R. Santbergen, O. Isabella, J. Schmitz, M. Lenes, J.M. Luchies, W.M.M. Kessels, I. Romijn, Material properties of LPCVD processed n-type polysilicon passivating contacts and its application in PERPoly industrial bifacial solar cells, in: *Energy Procedia*, Elsevier Ltd, 2017: pp. 635–642. <https://doi.org/10.1016/j.egypro.2017.09.250>.
- [14] P. Padhamnath, J.K. Buatis, A. Khanna, N. Nampalli, N. Nandakumar, V. Shanmugam, A.G. Aberle, S. Duttagupta, Characterization of screen printed and fire-through contacts on LPCVD based passivating contacts in monoPoly™ solar cells, *Sol. Energy*. 202 (2020) 73–79. <https://doi.org/10.1016/j.solener.2020.03.087>.
- [15] P. Padhamnath, A. Khanna, N. Nandakumar, N. Nampalli, V. Shanmugam, A.G. Aberle, S. Duttagupta, Development of thin polysilicon layers for application in monoPoly™ cells with screen-printed and fired metallization, *Sol. Energy Mater. Sol. Cells*. 207 (2020). <https://doi.org/10.1016/j.solmat.2019.110358>.
- [16] P. Padhamnath, A. Khanna, N. Balaji, V. Shanmugam, N. Nandakumar, D. Wang, Q. Sun, M. Huang, S. Huang, B. Fan, B. Ding, A.G. Aberle, S. Duttagupta, Progress in screen-printed metallization of industrial solar cells with SiOx/poly-Si passivating contacts, *Sol. Energy Mater. Sol. Cells*. 218 (2020) 110751. <https://doi.org/10.1016/j.solmat.2020.110751>.
- [17] T. Kamins, *Polycrystalline Silicon for Integrated Circuits and Displays*, Springer US, 1998. <https://doi.org/10.1007/978-1-4615-5577-3>.
- [18] A.J. Learn, D.W. Foster, Deposition and electrical properties of in situ phosphorus-doped silicon films formed by low-pressure chemical vapor deposition, *J. Appl. Phys.* 61 (1987) 1898–1904. <https://doi.org/10.1063/1.338036>.
- [19] B.S. Meyerson, W. Olbricht, Phosphorus-Doped Polycrystalline Silicon via LPCVD: I. Process Characterization, *J. Electrochem. Soc.* 131 (1984) 2361–2365. <https://doi.org/10.1149/1.2115258>.
- [20] B.S. Meyerson, M.L. Yu, Phosphorus-Doped Polycrystalline Silicon via LPCVD: II. Surface Interactions of the Silane/Phosphine/Silicon System, *J. Electrochem. Soc.* 131

- (1984) 2366–2368. <https://doi.org/10.1149/1.2115259>.
- [21] J.G.M. Mulder, P. Eppenga, M. Hendriks, J.E. Tong, An Industrial LPCVD Process for In Situ Phosphorus-Doped Polysilicon, *J. Electrochem. Soc.* 137 (1990) 273–279. <https://doi.org/10.1149/1.2086381>.
- [22] W. Ahmed, E. Ahmed, An Investigation of LPCVD and PECVD of in situ Doped Polycrystalline Silicon for VLSI, *Adv. Mater. Opt. Electron.* 1 (1992) 255–259. <https://doi.org/10.1002/amo.860010508>.
- [23] R.C.G. Naber, B.W.H. Van De Loo, J.R.M. Luchies, LPCVD In-situ N-type Doped Polysilicon Process Throughput Optimization and Implementation into an Industrial Solar Cell Process Flow, in: 36th Eur. Photovolt. Sol. Energy Conf. Exhib., 2019: pp. 180–183. <https://doi.org/10.4229/EUPVSEC20192019-2BO.3.2>.
- [24] A. Lanterne, J. Yang, J.-C. Loretz, B. Martel, M. Caruel, N. Enjalbert, H. Lignier, S. Dubois, LPCV-Deposited Poly-Si Passivated Contacts: Surface Passivation, Gettering and Integration in High Efficiency Devices, in: Proc. IEEE 47th Photovolt. Spec. Conf., 2020. <https://doi.org/10.1109/PVSC45281.2020.9300425>.
- [25] A. Lanterne, J. Yang, J.-C. Loretz, R. Monna, N. Enjalbert, B. Martel, S. Benguesmia, C. Lorfeuvre, C. Denis, S. Dubois, Phosphorus Doped Poly-Si Passivated Contacts by LPCVD and PECVD for Industrial Large-Area Solar Cells, in: Proc. 37th Eur. Photovolt. Sol. Energy Conf. Exhib., 2020: pp. 570–573. <https://doi.org/10.4229/EUPVSEC20202020-2DV.3.54>.
- [26] M. Firat, H. Sivaramakrishnan Radhakrishnan, M. Recamán Payo, F. Duerinckx, L. Tous, J. Poortmans, In situ phosphorus-doped polycrystalline silicon films by low pressure chemical vapor deposition for contact passivation of silicon solar cells, 231 (2022) 78–87. <https://doi.org/10.1016/j.solener.2021.11.045>.
- [27] B. Kafle, B.S. Goraya, S. Mack, F. Feldmann, S. Nold, Solar Energy Materials and Solar Cells TOPCon – Technology options for cost efficient industrial manufacturing, *Sol. Energy Mater. Sol. Cells.* 227 (2021) 111100. <https://doi.org/10.1016/j.solmat.2021.111100>.
- [28] A. Ingenito, G. Nogay, Q. Jeangros, E. Rucavado, C. Allebé, S. Eswara, N. Valle, T. Wirtz, J. Horzel, T. Koida, M. Morales-Masis, M. Despeisse, F.J. Haug, P. Löper, C. Ballif, A passivating contact for silicon solar cells formed during a single firing thermal annealing, *Nat. Energy.* 3 (2018) 800–808. <https://doi.org/10.1038/s41560-018-0239-4>.
- [29] E. Cornagliotti, A. Uruena, J. Horzel, J. John, L. Tous, D. Hendrickx, V. Prajapati, S.

- Singh, R. Hoyer, F. Delahaye, K. Weise, D. Queisser, H. Nussbaumer, J. Poortmans, How Much Rear Side Polishing is Required? A Study on the Impact of Rear Side Polishing in PERC Solar Cells, in: Proc. 27th Eur. Photovolt. Sol. Energy Conf. Exhib., 2012: pp. 561–566. <https://doi.org/10.4229/27thEUPVSEC2012-2AO.1.6>.
- [30] Q. Wang, W. Wu, D. Chen, L. Yuan, S. Yang, Y. Sun, Q. Zhang, Y. Cao, H. Qu, N. Yuan, J. Ding, Study on the cleaning process of n⁺-poly-Si wraparound removal of TOPCon solar cells, Sol. Energy. 211 (2020) 324–335. <https://doi.org/10.1016/j.solener.2020.09.028>.
- [31] E. Cornagliotti, M. Ngamo, L. Tous, R. Russell, J. Horzel, D. Hendrickx, B. Douhard, V. Prajapati, T. Janssens, J. Poortmans, Integration of inline single-side wet emitter etch in PERC cell manufacturing, Energy Procedia. 27 (2012) 624–630. <https://doi.org/10.1016/j.egypro.2012.07.120>.
- [32] N. Sahouane, A. Zerga, I. Bensefia, Influence Of SiNx: H And SiO_x Films On Optical And Electrical Properties Of Antireflective Coatings For Silicon Solar Cells, Int. J. Sci. Technol. Res. 3 (2014) 7–12.
- [33] N. Nandakumar, J. Rodriguez, T. Kluge, T. Große, L. Fondop, P. Padhamnath, N. Balaji, M. König, S. Duttagupta, Approaching 23% with large-area monoPoly cells using screen-printed and fired rear passivating contacts fabricated by inline PECVD, Prog. Photovoltaics Res. Appl. 27 (2019) 107–112. <https://doi.org/10.1002/pip.3097>.
- [34] S. Bowden, A. Rohatgi, Rapid and Accurate Determination of Series Resistance and Fill Factor Losses in Industrial Silicon Solar Cells, in: Proc. 17th Eur. Photovolt. Sol. Energy Conf. Exhib., 2001.
- [35] C. Comparotto, J. Theobald, J. Lossen, V.D. Mihailetchi, Understanding Contact Formation on n-PERT-RJ Solar Cells, in: 33rd Eur. Photovolt. Sol. Energy Conf. Exhib., 2017: pp. 832–836. <https://doi.org/10.4229/EUPVSEC20172017-2CV.2.23>.
- [36] T. Söderström, P. Papet, J. Ufheil, Smart Wire Connection Technology, in: Proc. 28th Eur. Photovolt. Sol. Energy Conf. Exhib., 2013: pp. 495–499. <https://doi.org/10.4229/28thEUPVSEC2013-1CV.2.17>.
- [37] A. Fell, A Free and Fast Three-Dimensional/Two-Dimensional Solar Cell Simulator Featuring Conductive Boundary and Quasi-Neutrality Approximations, IEEE Trans. Electron Devices. 60 (2013) 733–738. <https://doi.org/10.1109/TED.2012.2231415>.
- [38] M. Firat, M.R. Payo, F. Duerinckx, J.M. Luchies, M. Lenes, J. Poortmans, Characterization of absorption losses in rear side N-type polycrystalline silicon passivating contacts, AIP Conf. Proc. 2147 (2019). <https://doi.org/10.1063/1.5123831>.

- [39] F. Feldmann, M. Nicolai, R. Müller, C. Reichel, M. Hermle, Optical and electrical characterization of poly-Si/SiO_x contacts and their implications on solar cell design, in: *Energy Procedia*, Elsevier Ltd, 2017: pp. 31–37.
<https://doi.org/10.1016/j.egypro.2017.09.336>.
- [40] S. Reiter, N. Koper, R. Reineke-Koch, Y. Larionova, M. Turcu, J. Krügener, D. Tetzlaff, T. Wietler, U. Höhne, J.D. Kähler, R. Brendel, R. Peibst, Parasitic Absorption in Polycrystalline Si-layers for Carrier-selective Front Junctions, in: *Energy Procedia*, Elsevier Ltd, 2016: pp. 199–204. <https://doi.org/10.1016/j.egypro.2016.07.057>.
- [41] H.E. Çiftçinar, M.K. Stodolny, Y. Wu, G.J.M. Janssen, J. Löffler, J. Schmitz, M. Lenes, J.M. Luchies, L.J. Geerligs, Study of screen printed metallization for polysilicon based passivating contacts, in: *Energy Procedia*, Elsevier Ltd, 2017: pp. 851–861. <https://doi.org/10.1016/j.egypro.2017.09.242>.
- [42] A. Chaudhary, J. Hoß, J. Lossen, R. Van Swaaij, M. Zeman, Screen printed Ag contacts for n-type polysilicon passivated contacts, *AIP Conf. Proc.* 2147 (2019). <https://doi.org/10.1063/1.5123829>.
- [43] A. Chaudhary, J. Hoß, J. Lossen, F. Huster, R. Kopecek, R. van Swaaij, M. Zeman, Influence of Polysilicon Thickness on Properties of Screen-Printed Silver Paste Metallized Silicon Oxide/Polysilicon Passivated Contacts, *Phys. Status Solidi Appl. Mater. Sci.* 218 (2021) 1–9. <https://doi.org/10.1002/pssa.202100243>.
- [44] K.R. McIntosh, L.P. Johnson, Recombination at textured silicon surfaces passivated with silicon dioxide, *J. Appl. Phys.* 105 (2009). <https://doi.org/10.1063/1.3153979>.
- [45] K. Bothe, C. Kruse, D. Hinken, R. Brendel, M. Rauer, J. Hohl-Ebinger, Contacting of Busbarless Solar Cells for Accurate I-V Measurements, in: *Proc. 37th Eur. Photovolt. Sol. Energy Conf. Exhib.*, 2020: pp. 277–281.
<https://doi.org/10.4229/EUPVSEC20202020-2CO.15.2>.
- [46] Y. Zhang, J. Xu, J. Mao, J. Tao, H. Shen, Y. Chen, Z. Feng, P.J. Verlinden, P. Yang, J. Chu, Long-term reliability of silicon wafer-based traditional backsheet modules and double glass modules, *RSC Adv.* 5 (2015) 65768–65774.
<https://doi.org/10.1039/c5ra11224a>.
- [47] P.P. Altermatt, Y. Yang, Y. Chen, X. Zhang, D. Chen, G. Xu, Z. Feng, Requirements of the Paris Climate Agreement for the Coming 10 Years on Investments, Technical Roadmap, and Expansion of PV Manufacturing, in: *Proc. 37th Eur. Photovolt. Sol. Energy Conf. Exhib.*, 2020: pp. 1999–2004.
<https://doi.org/10.4229/EUPVSEC20202020-7CP.1.2>.

- [48] P. Choulat, S. Singh, L. Tous, J. Chen, Z. Liu, F. Duerinckx, I. Gordon, J. Szlufcik, Exceeding 23% Screen-Printed Rear-Emitter Bifacial N-PERT Cells, in: Proc. 36th Eur. Photovolt. Sol. Energy Conf. Exhib., 2019; pp. 157–160.
<https://doi.org/10.4229/EUPVSEC20192019-2BO.1.4>.
- [49] D.L. Young, K. Chen, S. Theingi, V. LaSalvia, D. Diercks, H. Guthrey, W. Nemeth, M. Page, P. Stradins, Reactive ion etched, self-aligned, selective area poly-Si/SiO₂ passivated contacts, Sol. Energy Mater. Sol. Cells. 217 (2020) 110621.
<https://doi.org/10.1016/j.solmat.2020.110621>.
- [50] P. Wang, R. Sridharan, X.R. Ng, A. Khanna, S. Venkataraj, R. Stangl, Investigating Industrial Metallization Solutions for Double-side Contact Passivated biPoly Solar Cells, Proc. 2019 IEEE 46th Photovolt. Spec. Conf. (2019) 1143–1147.
<https://doi.org/10.1109/PVSC40753.2019.8980500>.